Geophys. J. Int. (2000) **143,** 395–406

Generation of microcracks by dynamic shear rupture and its effects on rupture growth and elastic wave radiation

Teruo Yamashita

Earthquake Research Institute, University of Tokyo, 1-1-1 *Yayoi, Bunkyo-ku, Tokyo* 113-0032, *Japan. E-mail: tyama@eri.u-tokyo.ac.jp*

Accepted 2000 May 30. Received 2000 May 21; in original form 1999 November 30

SUMMARY

Laboratory and field observations suggest that dynamically propagating earthquake faults generate a large number of tensile microcracks in their vicinity, which will contribute to the formation of fault zones. Intense interactions are expected to occur between such microcracks and a dynamically propagating fault, which will complicate the fault growth. Near-field seismic waves will also be affected by the generation of microcracks. We numerically study how such tensile microcracks are generated and how dynamic growth of a macroscopic shear rupture and near-field elastic waves are affected by the distribution of generated microcracks. It is essential to consider a large number of microcracks in such studies, so that it is impractical to consider each microcrack individually from the viewpoint of computation time and memory. We overcome this difficulty by representing the microcrack distribution by anisotropic properties of the overall elastic coefficients on the basis of Hudson's (1980) study. Our simulations show that the decrease in the microcrack density is approximated well by a logarithmic function of the distance from the rupture plane. Microcracks on the dilational side of the rupture plane are shown to make larger angles to the rupture plane than on the compressive side. These are consistent with field and laboratory observations. It is also shown that dynamically generated microcracks tend to reduce the rupture-tip shear stress. This implies that the dynamic growth of a shear rupture is more decelerated when microcracks are generated than when the shear rupture is isolated in an isotropic and homogeneous medium. If the dynamic rupture growth is arrested suddenly, an abrupt expansion of the distribution zone of microcracks is shown to occur near the arrested rupture tip. Aftershocks are expected to cluster in this zone because of the shear stress enhancement there and the high density of distributed microcracks, which facilitates aftershock occurrence due to dynamic coalescence of microcracks. Our simulations also show that the component of radiated displacement waves perpendicular to the rupture plane is much more affected by the generation of microcracks than the parallel component.

Key words: anisotropy, cracked media, earthquake, faulting, fractures, rupture propagation.

INTRODUCTION

It is now increasingly clear that the characterization of faults as discrete planar surfaces is inappropriate (e.g. Kame & Yamashita 1997, 1999a,b; Vermilye & Scholz 1998). In fact, it is well known that a major crustal fault is not a single fault but forms a fault zone (e.g. Tchalenko 1970; Engelder 1974; Chester *et al.* 1993; Tchalenko & Berberian 1975; Caine *et al.* 1996). Rocks are greatly damaged in and near fault zones and microfractures are highly developed there. There have been many studies documenting the concentration of microfractures near earthquake faults (e.g. Gangi *et al.* 1977; Anders & Wiltschko 1994; Scholz *et al.* 1993). Anders & Wiltschko (1994) took cores at different distances from a number of faults in their field investigation. They measured both microcrack orientation and microcrack density. All microcracks they studied were tensile. In addition, they observed a rapid decrease in the microcrack density with distance from the fault in all the

examples. Vermilye & Scholz (1998) observed, in a field investigation of brittle faults, that tensile microcracks have features reflecting the stress field caused by propagating shear-rupture tips.

In their laboratory experiments, Moore & Lockner (1995) investigated microcracking related to the growth of a shear fracture in a Westerly granite. Their observations are consistent with those of Anders & Wiltschko (1994): they found that microcracks formed during the experiment are principally tensile cracks, and observed a rapid drop-off in microcrack density with increasing distance from the fault. They also observed a high concentration of microcracks near the propagating fault tip, which is because of the significant stress enhancement there. The microcrack density was found to be higher on the dilational side of the fault, and the orientation of the cracks was generally consistent with tensile cracks. Petit & Barquins (1988) observed a shear zone consisting of tensile microcracks developed from the tip of a pre-existing joint in their laboratory experiments with polymethylmethacrylate (PMMA) and sandstone. They suggested on the basis of their experiments that mode II shear can only be a macroscopic rupture phenomenon that must necessarily involve tensile microcrack formation.

The above laboratory and field observations suggest that propagating earthquake faults can generate a large number of tensile microcracks in their vicinity. Intense interactions are expected to occur between such microcracks and a propagating fault, which will complicate the fault growth. It will be impractical to analyse each microcrack individually in numerical simulations of the generation of microcracks because of the limitations of computer memory and CPU time. We now try to overcome this limitation by employing a new approach.

It has been shown mathematically that a weak concentration of oriented microcracks in an elastic body can be represented by the overall effective elastic coefficients having anisotropic properties (e.g. Hudson 1980, 1981). We apply the formula derived by Hudson (1980) for microcracks aligned in a single direction to the case of microcracks generated by dynamic shear rupture. This assumes that the microcracks are locally parallel. This assumption will be approximately valid when the spatial variation of the microcrack orientation has wavelengths much larger than the sizes of the microcracks. We also assume that the sizes of the microcracks and their separation distances are less than the wavelengths of a propagating elastic wave, which was assumed by Hudson (1980, 1981) in his analysis. In addition, the concentration of microcracks must be dilute. In spite of these limitations, our approach has the advantage that we can easily treat spatio-temporal changes in the distribution of a large number of microcracks. Our approach also has the advantage that the concept of a breakdown zone at rupture tips is naturally introduced by the spatio-temporal change of anisotropic properties of the effective elastic coefficients near the propagating rupture tips. While the breakdown process is assumed to occur entirely within the rupture plane in many theoretical and numerical analyses, mainly because of mathematical simplicity (e.g. Yamashita & Ohnaka 1991; Vermilye & Scholz 1998), we can easily treat the breakdown process occurring within a volume of rock surrounding the rupture tip in our present approach.

The purpose of this paper is to investigate numerically how tensile microcracks are generated and how the dynamic growth of a macroscopic shear rupture and radiated elastic waves are affected by the distribution of microcracks formed in the vicinity of the rupture. We consider both pre-existing microcracks and those generated by the dynamic growth of a shear rupture. It will be shown that the microcracks generated by the dynamic growth of rupture tend to reduce the rupture-tip shear stress. This implies that the generation of microcracks tends to decelerate dynamic fault growth. It will be shown that the spatial distribution of the generated microcracks is in good agreement with field and laboratory observations. It is also shown that the component of radiated displacement waves perpendicular to the rupture plane is affected considerably by the generation of microcracks.

MATHEMATICAL TREATMENT OF MICROCRACKS

Assume 2-D plane strain elastic deformation on the plane x_1x_3. When dilutely distributed microcracks are aligned in the direction of the x'_1-axis (Fig. 1), the constitutive relation is written as

$$\begin{aligned} p_{ij} &= c_{ijkl}e_{kl} \qquad (i, j, k, l = 1, 3), \\ c_{ijkl} &= l_{ri}l_{sj}l_{pk}l_{ql}c'_{rspq} \qquad (i, j, k, l, r, s, p, q = 1, 3) \end{aligned} \tag{1}$$

in the coordinate system x_1x_3, where p_{ij} and e_{kl} are components of the stress and strain tensors, c_{ijkl} are the elastic coefficients and l_{ij} denotes the cosine of the angle between the x_j- and x'_i-axes. Einstein's summation convention is applied to repeated indices unless noted otherwise. Tensile stresses are assumed to be positive in our formulation. In eq. (1), c'_{ijkl} are the effective elastic coefficients, associated with the coordinate system $x'_1x'_3$, applicable to the propagation of long-wavelength elastic waves through a solid permeated by microcracks aligned in the direction of the x'_1-axis, and they are written in the form (Hudson 1980, 1981)

$$c'_{ijkl} = c^{0\prime}_{ijkl} + c^{1\prime}_{ijkl}\,, \tag{2}$$

where $c^{1\prime}_{ijkl}$ are the first-order perturbations of the isotropic elastic coefficients $c^{0\prime}_{ijkl}[=\mu(\delta_{ik}\delta_{jl}+\delta_{il}\delta_{jk})+\lambda\delta_{ij}\delta_{kl}]$ of the uncracked solid. In other words, $c^{1\prime}_{ijkl}$ are linearly proportional to the microcrack density $\varepsilon \equiv Na^2/V$, where N is the number of

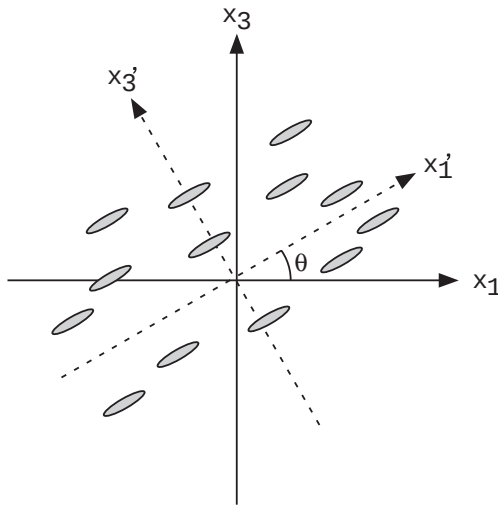

Figure 1. The coordinate system x_1x_3 assumed in this paper. Tensile microcracks are aligned in the x'_1-direction.

microcracks with length $2a$ in volume V in an isotropic solid with the Lamé constants λ and μ. While Hudson (1980) derived the expression for the effective elastic coefficients up to the second-order perturbations, we use them only up to the first-order perturbation because of qualitative consideration of the effect of microcracks and the assumption of a dilute distribution of microcracks. Each microcrack is assumed to be tensile, as observed in field and laboratory investigations, and a traction-free boundary condition is assumed on each microcrack. The explicit expression for the elastic coefficients $c^{1\prime}_{ijkl}$ is found in Hudson (1980).

We now regard the microcrack orientation θ (Fig. 1) as a function of space and its density ε as a function of both space and time. This enables us to consider the spatio-temporal variation of microcrack distribution. As stated in the Introduction, the spatial variation of the microcrack orientation must have wavelengths much larger than the lengths of the microcracks to apply the formula of Hudson (1980). We assume that a tensile microcrack is generated if a tensile stress component exceeds a certain threshold. In other words, a tensile microcrack is generated with its plane in the x'_1 direction if the condition

$$p'^{(\max)}_{33} > c_0 \tag{3}$$

is satisfied, where c_0 is the threshold for the generation of the microcrack and $p'^{(\max)}_{33}$ denotes the maximum tensile stress p'_{33} at a fixed location on the $x'_1x'_3$-plane. The coordinate system $x'_1x'_3$ is assumed as the local coordinates to represent the orientation of each microcrack (Fig. 1). Primed quantities stand for those associated with the coordinate system $x'_1x'_3$. The direction of the x'_3-axis is determined by the conditions

$$dp'^{(\max)}_{33}/d\theta = 0 \quad \text{and} \quad d^2p'^{(\max)}_{33}/d\theta^2 < 0\,. \tag{4}$$

Condition (3) can then be rewritten in the following form in the global coordinate system x_1x_3:

$$\frac{p_{11}+p_{33}}{2} + \sqrt{p_{13}^2 + \frac{(p_{11}-p_{33})^2}{4}} > c_0\,. \tag{3'}$$

It is reasonable to assume that each nucleated microcrack grows in size with increasing p'_{33} in the range $p'_{33} > c_0$. Hence, we assume the following relation rather arbitrarily:

$$\varepsilon = \varepsilon_0[1 - \exp(-(p'_{33}-c_0)/\alpha)]\,, \tag{5}$$

where ε_0 is the upper limit for the microcrack density and α is a positive constant. We here assume that each microcrack grows in its own plane, that is, the orientation of each crack is fixed at the instant when it nucleates. The elastic coefficients c_{ijkl} are determined at any location once the crack density ε and the crack orientation are given there. Since the first-order perturbation is assumed for the crack density, ε_0 must be small. The difference between results given by the first- and second-order perturbations seems to be negligible for $\varepsilon \le 0.05$ (Hudson & Crampin 1991), so that we assume $\varepsilon_0 \le 0.05$ in all the following calculations. Differences in the assumed form of the dependence of the microcrack density on the stress p'_{33} will not affect the calculated results much since the microcrack density is low and its spatial distribution is smooth, as is shown later.

FINITE DIFFERENCE FORMULATION

The equation of motion is written in the form

$$\rho\,\frac{\partial^2}{\partial t^2}\,u_i = \frac{\partial}{\partial x_1}\,p_{1i} + \frac{\partial}{\partial x_3}\,p_{3i} \quad (i=1,\,3) \tag{6}$$

in the global coordinate system x_1x_3, where ρ is the density of the medium and u_i is the ith component of the displacement vector. We solve eq. (6) by the finite difference method. The time derivative on the left-hand side can be approximated by the second-order central difference. However, some care must be taken with the calculation of the right-hand side since the elastic coefficients are functions of the spatial coordinates in our modelling (Boore 1972; Kelly *et al.* 1976). The stress tensor components are written as

$$p_{ij} = \frac{1}{2}\,c_{ijkl}\left(\frac{\partial u_k}{\partial x_l} + \frac{\partial u_l}{\partial x_k}\right) \quad (i,\,j,\,k,\,l=1,\,3) \tag{7}$$

in terms of the displacement components, so that we must consider two types of terms that occur on the right-hand side of eq. (6), specifically those having partial derivatives with respect to one spatial coordinate only and those containing partial derivatives with respect to both spatial variables. These terms are discretized following the treatment of Kelly *et al.* (1976), which was found to perform satisfactorily. For example, a term typical of the first type,

$$\frac{\partial}{\partial x_1}\left[a(x_1,\,x_3)\,\frac{\partial u}{\partial x_1}\right], \tag{8}$$

is discretized in the form

$$\frac{(a_{i+1,j}+a_{i,j})(u_{i+1,j}-u_{i,j}) - (a_{i-1,j}+a_{i,j})(u_{i,j}-u_{i-1,j})}{2h^2} \tag{9}$$

at $x_1 = ih$ and $x_3 = jh$, where i, j are integers, h is the grid interval in both the x_1- and the x_3-directions, $b_{i,j} = b(ih,\,jh)$ ($b = a$ or u), and a and u denote an elastic coefficient and a displacement vector component, respectively. Refer to Kelly *et al.* (1976) for details concerning the discretization of other terms on the right-hand side of eq. (6).

INITIAL AND BOUNDARY CONDITIONS FOR FINITE DIFFERENCE SIMULATION

We assume a uniform stress state, $p_{11} = p_{33} = t_0 (<0)$ and $p_{13} = s_0 (>0)$, at $t=0$, and the relative change from this state is simulated below. The condition (3′) becomes

$$\frac{p^d_{11}+p^d_{33}}{2} + \sqrt{(s_0+p^d_{13})^2 + \frac{(p^d_{11}-p^d_{33})^2}{4}} > c_0 - t_0 \equiv c_1\,, \tag{3''}$$

where the superscript d denotes the perturbation from the initial static state. The condition (3″) suggests that the initial compressive stress t_0 contributes to the microcrack generation condition only implicitly. The superscript d is discarded in the following for brevity. The number of gridpoints is assumed to be sufficiently large that waves reflected from the remote grid boundary cannot affect the numerical results.

We now assume that a shear rupture is nucleated dynamically at $t=+0$ and then propagates bilaterally along the plane $x_3=-h/2$ from the origin; this is referred to as the main crack. The main crack is assumed to generate tensile microcracks in its vicinity. If the medium were isotropic and the elastic coefficients were independent of the spatial coordinates, the numerical treatment of boundary conditions for the analysis of the main crack would be much simpler than ours. In other words, we can consider only a half-plane, $x_3\geq -h/2$ (or $x_3\leq -h/2$), in such modelling because of symmetrical deformation about the plane $x_3=-h/2$ (e.g. Alterman *et al.* 1971). However, such symmetry cannot be expected in our modelling, so that some care must be taken about boundary conditions on the plane of the main crack.

First, the stresses p_{13} and p_{33} and the displacement u_3 must be continuous across the plane $x_3=-h/2$. Since the shear stress p_{13} is released on the main crack, we also have the condition

$$p_{13}(x_1, t)=-\triangle\sigma(x_1, t) \quad \text{for} \quad a(t)<x_1<b(t) \quad \text{and} \quad x_3=-h/2, \tag{10}$$

where $\triangle\sigma$ is the magnitude of the shear stress released on the main crack, and $a(t)$ and $b(t)$ are the locations of the left and right tips of the main crack at time t. Finally, the displacement component u_1 must be continuous across the plane $x_3=-h/2$ for $x_1>b(t)$ and $x_1<a(t)$. We now derive numerical expressions for these conditions. As long as the equation of motion is formulated in term of the displacement vector as in our case, it seems necessary to introduce fictitious gridpoints immediately above and below the plane of the main crack for a finite difference simulation of its growth (e.g. Alterman *et al.* 1971). Such fictitious gridpoints are now introduced at $x_3=-h$ and $x_3=0$ for the analysis of the deformation on the upper $x_3>-h/2$ and lower $x_3<-h/2$ planes, respectively (Fig. 2). It should be noted that we have both fictitious and non-fictitious gridpoints at the locations $x_3=-h$ and $x_3=0$. For example, the fictitious gridpoints at $x_3=-h$ are used for the analysis of deformation on the upper plane, $x_3>-h/2$, while the non-fictitious gridpoints there are used for the analysis of the deformation on the lower plane, $x_3<-h/2$.

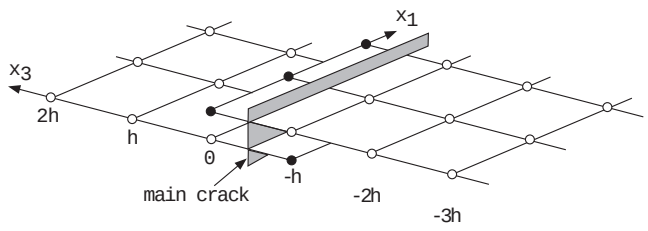

Figure 2. Arrangement of the gridpoints near the plane of the main crack. Open and closed circles denote the non-fictitious and fictitious gridpoints, respectively. The main crack is located on the plane $x_3=-h/2$.

The boundary conditions are thus numerically represented as

$$c_{1333}(i, 0)\frac{w_{i+1,0}-w_{i-1,0}}{2h}+c_{1313}(i, 0)\frac{u_{i,0}-u^*_{i,-1}}{h}+c_{1311}(i, 0)\frac{u_{i+1,0}-u_{i-1,0}}{2h}+c_{1333}(i, 0)\frac{w_{i,0}-w^*_{i,-1}}{h}=\triangle\sigma, \tag{11a}$$

$$c_{1333}(i, -1)\frac{w_{i+1,-1}-w_{i-1,-1}}{2h}+c_{1313}(i, -1)\frac{u^*_{i,0}-u_{i,-1}}{h}+c_{1311}(i, -1)\frac{u_{i+1,-1}-u_{i-1,-1}}{2h}+c_{1333}(i, -1)\frac{w^*_{i,0}-w_{i,-1}}{h}=\triangle\sigma, \tag{11b}$$

$$c_{3311}(i, 0)\frac{u_{i+1,0}-u_{i-1,0}}{2h}+c_{3333}(i, 0)\frac{w_{i,0}-w^*_{i,-1}}{h}+c_{3313}(i, 0)\frac{w_{i+1,0}-w_{i-1,0}}{2h}+c_{3313}(i, 0)\frac{u_{i,0}-u^*_{i,-1}}{h}=c_{3311}(i, -1)\frac{u_{i+1,-1}-u_{i-1,-1}}{2h}+c_{3333}(i, -1)\frac{w^*_{i,0}-w_{i,-1}}{h}+c_{3313}(i, -1)\frac{w_{i+1,-1}-w_{i-1,-1}}{2h}+c_{3313}(i, -1)\frac{u^*_{i,0}-u_{i,-1}}{h}, \tag{11c}$$

$$\frac{w^*_{i,0}+w_{i,-1}}{2}=\frac{w^*_{i,-1}+w_{i,0}}{2}, \tag{11d}$$

for $i_p\leq i\leq i_q$, where $u=u_1$ and $w=u_3$, the main crack is assumed to be located in the range $i_ph\leq x_1\leq i_qh$, $c_{ijkl}(m, n)$ are the values of c_{ijkl} at $x_1=mh$ and $x_3=nh$ and the asterisk denotes the values at the fictitious gridpoints. Eqs (11a) and (11b) represent the condition (10) for the deformation on the upper and lower half-planes, respectively. Eqs (11c) and (11d) denote the continuity of p_{33} and u_3 across the plane $x_3=-h/2$, respectively. The quantities on the fictitious planes, $u^*_{i,0}$, $u^*_{i,-1}$, $w^*_{i,0}$ and $w^*_{i,-1}$, are determined from the above four equations.

We assume the continuity of u_1, u_3, p_{31} and p_{33} across the plane $x_3=-h/2$ outside the main crack, i.e., $i\geq i_q+1$ and $i\leq i_p-1$. These conditions can be discretized in the same way as in eq. (11) by introducing the fictitious gridpoints at $x_3=0$ and $-h$.

The physical quantities are normalized by an arbitrary unit of length L and the initial shear stress s_0 in the following calculations. The non-dimensional coordinates are therefore given by $X_i=x_i/L$ ($i=1$ and 3) and $T=V_pt/L$, where V_p is the P-wave velocity of the uncracked matrix solid. We set $dX=h/L=0.5$ and $dT=V_p\triangle t/L=0.2$ in the following calculations, where $\triangle t$ is a time increment in the finite difference calculation of eq. (6).

The accuracy of our method of analysis is investigated by comparing our numerical solution for the self-similar crack growth problem with the analytical one given by Kostrov (1964). It is shown in Appendix A that the agreement between the two solutions is satisfactory.

GENERATION OF MICROCRACKS BY DYNAMIC RUPTURE GROWTH

The remotely applied shear stress $p_{13}=s_0$ is assumed to be completely released on the main crack, so that $\triangle\sigma=s_0$. The generation of the microcracks is represented by the spatio-temporal change of anisotropic properties of the effective elastic coefficients in our modelling, as stated before. The parameter α in eq. (5) is fixed at $\alpha/s_0=5.0$ in all the following calculations. Since the stresses are obtained by the numerical differentiation of the displacement vector in our treatment, short-wavelength numerical noise is inevitably superposed on the calculated stresses. We eliminate this noise by smoothing the calculated stresses to obtain a smooth distribution of the value of the left-hand side of the condition (3″) except at the grid-points immediately ahead of the tips of the main crack and at their eight nearest-neighbour gridpoints; the smoothed value of stress at a certain gridpoint is obtained by averaging the stresses over it and its eight nearest-neighbour gridpoints.

The orientation and density of the microcracks are shown in Fig. 3; the tips of the main crack are assumed to extend with a fixed velocity $v_r=0.4V_p(=0.69V_s)$, where V_p and V_s are the *P*- and *S*-wave velocities of the uncracked matrix solid. Only the half-plane $x_1>0$ is illustrated here because of the symmetry of the deformation $u_1(x_1, x_3)=-u_1(-x_1, -x_3)$ and $u_3(x_1, x_3)=-u_3(-x_1, -x_3)$. The fracture zone, defined as the volume of rock containing microcracks generated by the propagation of the tips of the main crack, is shown to expand with the rupture growth in our simulations; the term 'fracture zone' is used fundamentally in the same way as in the process zone in Vermilye & Scholz (1998). Since the expression for the effective elastic coefficients c'^{1}_{ijkl} is derived assuming a homogeneous statistical distribution of the microcracks, it appears that the degree of approximation of the microcrack distribution by the anisotropic properties of the effective elastic coefficients may not be very high near the boundary of the fracture zone. However, the microcrack density is close to zero there, so that this will not influence the calculated results much.

Our calculations show that the fracture zone width, H_d, is larger when c_1 is smaller. Furthermore, as expected, a larger number of microcracks are generated on the dilational side of the main crack than on the compressive side (Fig. 3). It is

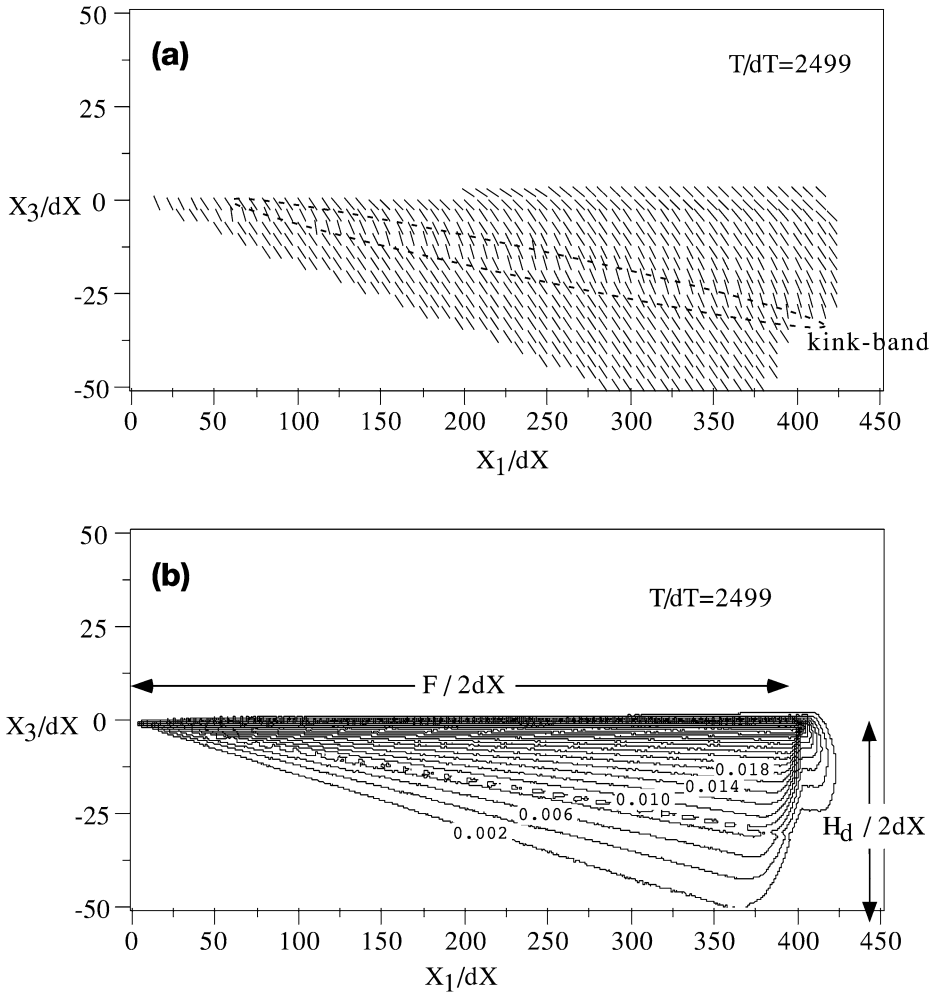

Figure 3. Distribution of microcracks in the fracture zone at time step $T/dT=2499$; $c_1/s_0=2.0$ and $v_r/V_p=0.4$ are assumed. The tip of the main crack lies at $X_1/dX=399$ at this instant. The length of the main crack is given by F, and H_d is the fracture zone width; note that the distribution of the microcracks is symmetrical with respect to the origin. (a) Orientation of microcracks. (b) Distribution of the microcrack density ε. Numerals denote the density.

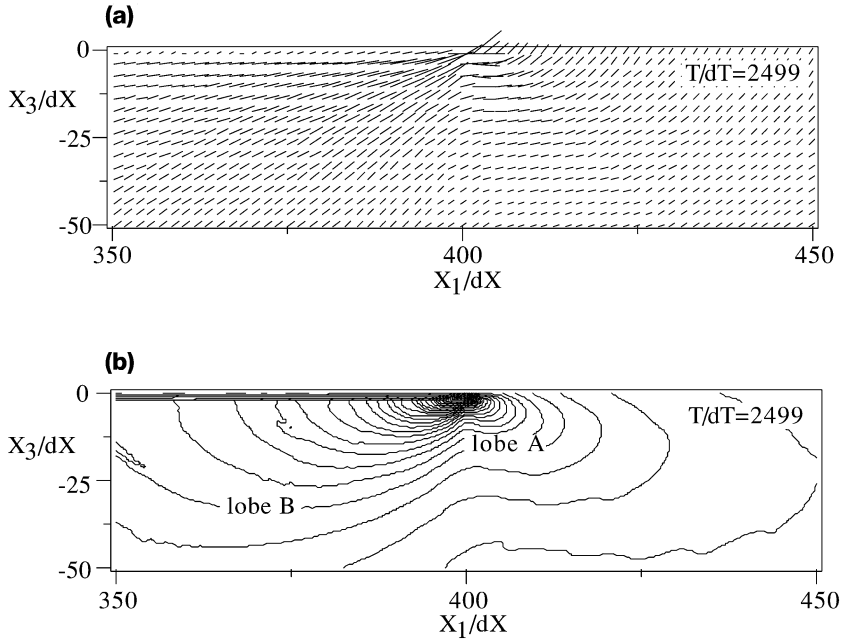

Figure 4. Distributions of (a) orientation and (b) magnitude of maximum tensile stress at time step $T/dT=2499$ near the tip of the main crack in the region $X_3 \leq 0$; no microcracks are assumed to be generated in these examples. The model of the main crack is the same as assumed in Fig. 3, so that the tip of the main crack lies at $X_1/dX=399$ at this instant. We observe that the magnitude of maximum tensile stress has a two-lobed distribution near the rupture tip: lobe A in front of the rupture tip and lobe B in the shadow of the rupture plane.

also observed in Fig. 3(a) that microcracks on the dilational side make larger angles to the main crack than those on the compressive side near the plane of the main crack, which is consistent with the laboratory observations of Moore & Lockner (1995). Fig. 3(a) clearly shows that the spatial change of the orientation of the microcracks is very smooth, which justifies our assumption of the representation of distributed microcracks in terms of the anisotropic properties of the effective elastic coefficients.

Microcrack orientations display a kink-like geometry within a narrow band through the fracture zone (Fig. 3a). This occurs because the orientation of each microcrack is fixed at the instant of its nucleation and $p_{33}^{(\max)}$ has a two-lobed distribution near the rupture tip: lobe A is in front of the rupture tip and lobe B is in the shadow of the rupture plane (Fig. 4b). Figs 4(a) and (b) show the distributions of orientation and magnitude of maximum tensile stress near the tip of the main crack in the uncracked isotropic medium. These figures suggest that microcracks nucleated in lobe A make larger angles to the main crack than those in lobe B. This will cause the kink-like change in the orientation of microcracks generated near the boundary between lobes A and B.

Fig. 5 shows that the decay of the microcrack density is well approximated by a logarithmic function of the distance from the rupture plane on the dilational side, which is also in good agreement with field observations (Anders & Wiltschko 1994; Vermilye & Scholz 1998); reliable estimation on the compressive side is difficult because of the generation of fewer microcracks.

Microcracks generated near the main crack give rise to a complicated stress field in its vicinity. Fig. 6(a) illustrates the temporal variation of the shear stress p_{31} at the gridpoint immediately ahead of the propagating tip of the main crack on its plane for some values of c_1 and ε_0; a stress component on the

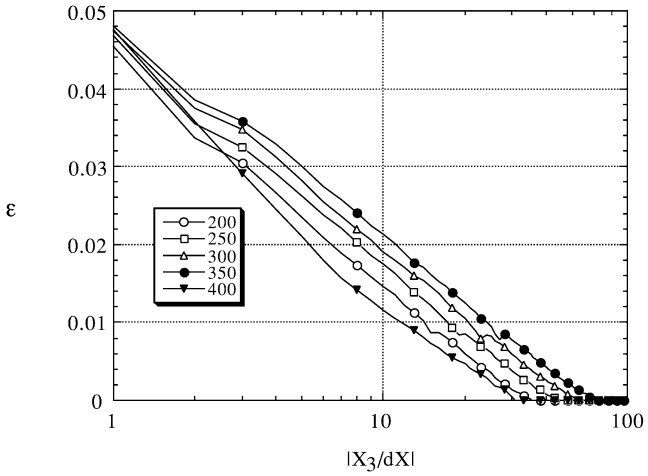

Figure 5. Decay of the microcrack density with distance from the rupture plane, on the dilational side, along the lines $X_1/dX=200$, 250, 300, 350 and 400 for the microcrack distribution shown in Fig. 3.

plane of the main crack $x_3=-h/2$ is obtained by averaging the calculated values on the planes at $x_3=0$ and $-h$. By virtue of the temporal and spatial discretization, the crack tip advances by one gridpoint only after several time steps have passed. The crack tip shear stress generally increases with time when the crack tip is stationary, while the stress suddenly drops once the tip advances to the gridpoint directly ahead. We illustrate in Fig. 6(a) the values of the crack tip shear stress taken immediately before the advancement of the crack tip. These values are the local maxima in the temporal variation. Fig. 6(a) shows that the reduction in the crack tip shear stress is larger

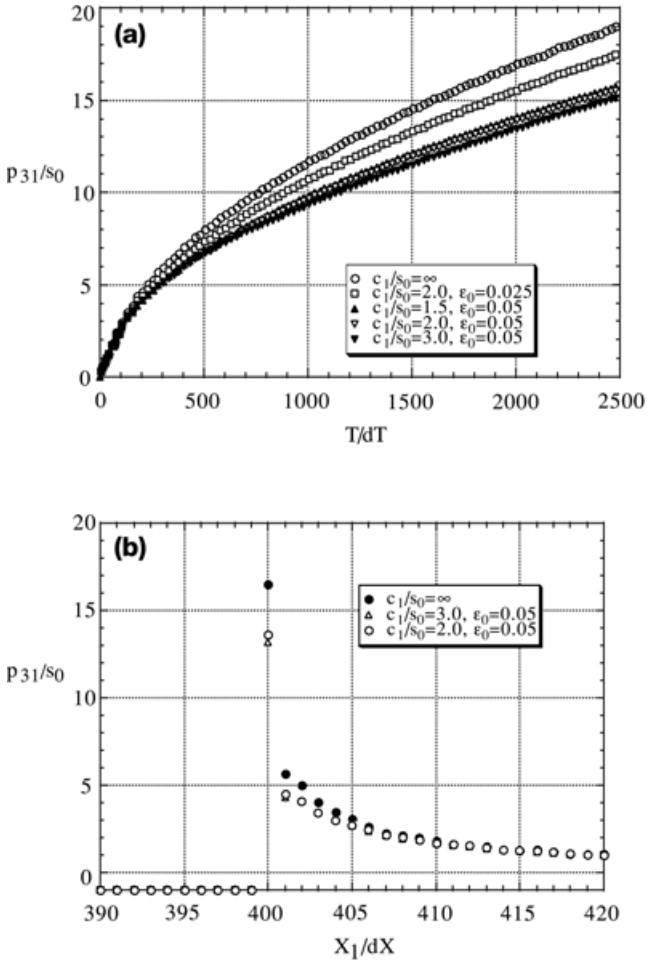

Figure 6. (a) Effects of c_1 and ε_0 on the temporal variation of the shear stress p_{31} immediately ahead of the propagating tip of the main crack. (b) Variation of p_{31} near the tip on the plane of the main crack at time step $T/dT=2499$. The crack tip advances to the gridpoint directly ahead at the next time step, so that the crack tip stress is enhanced at this instant.

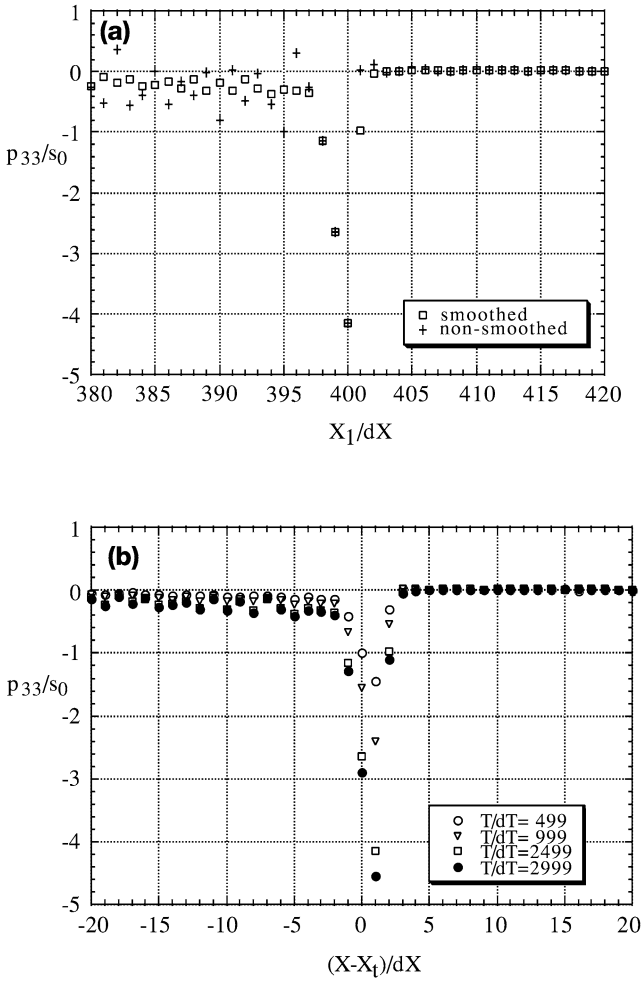

Figure 7. (a) Variation of the stress p_{33} near the crack tip on the plane of the main crack at time step $T/dT=2499$. The crack tip is located at $X_1/dX=399$ at this instant. The values obtained by smoothing are also shown; the smoothing is carried out except at the gridpoints immediately ahead of the tips of the main crack and at their eight nearest neighbour gridpoints. (b) Variation of p_{33} near the tip of the main crack at instants $T/dT=499$, 999, 2499 and 2999. The stress shown here is the smoothed one; X_t denotes the location of the crack tip. We assume $v_r/V_p=0.4$, $c_1/s_0=2.0$ and $\varepsilon_0=0.05$ in the examples shown here.

when ε_0 is larger (see also Fig. 6b). The numerical results have little dependence on the values of c_1 when ε_0 is fixed. The rate of the reduction in the crack tip shear stress is almost independent of T for large T when ε_0 is fixed. For example, the generation of microcracks with a threshold value $\varepsilon_0=0.05$ reduces the crack tip shear stress by about 18 per cent for $T/dT>1000$ in comparison with the case of a shear rupture growing in an uncracked medium.

The resolution of the calculated values of p_{31} seems to be satisfactory, especially on the plane of the main crack when considering the dependence of p_{31} on the model parameters, while larger numerical noise is found in the variation of p_{33}, as shown in Fig. 7(a)—compare this with Fig. 6(b). If we smooth p_{33} over the nearest-neighbour gridpoints, the noise is reduced greatly, while it is obvious even before smoothing that the stress p_{33} takes large negative values near the tip of the main crack (Fig. 7a). Our calculation shows that the reduction in the value of p_{33} is larger near the crack tip when ε_0 is larger. The reduction is enhanced with crack growth (Fig. 7b). It should be noted that if an isolated straight crack extends in an isotropic and homogeneous elastic medium, the stress p_{33} vanishes over the crack plane because of the symmetry properties of deformation (e.g. Burridge 1969; Alterman *et al.* 1971). Hence, the variation of p_{33} observed in Fig. 7 results from the formation of microcracks. Consideration of Figs 6 and 7 implies that if either the shear traction criterion or the Coulomb criterion is assumed as a fracture criterion, the growth of the main crack decelerates more when microcracks are generated.

Andrews & Ben-Zion (1997) observed self-sustaining propagation of slip pulses on a planar interface separating different elastic materials in their numerical simulations. This occurs because the change of normal traction is tensile during the propagating slip pulse. Although elastic properties are largely different above and below the plane of the main crack in our simulations too, such self-sustaining propagation of slip pulses is not observed. Rather, it is shown that the change of the normal traction is compressive near the tip of the main crack, which tends to impede the growth of a shear crack. The

difference in the simulation results occurs mainly because the elastic properties are inhomogeneous only near the main crack and are anisotropic in our modelling.

If the main crack grows bilaterally with a fixed velocity, as is assumed in Fig. 3, the width of the fracture zone should scale with the length of the main crack at any instant; this is confirmed in the simulations. For example, the ratio of the maximum width of the fracture zone, H_d, to the length of the main crack, F, is about 0.15 for $c_1/s_0=2.0$ and $v_r=0.4V_p$ for any T in the range $0\leq T/dT\leq 2500$, as is typically observed in Fig. 3(b); a slight tendency is found for this ratio to increase with decreasing crack tip velocity. The ratio is found to decrease with increasing c_1/s_0 for a fixed value of v_r/V_p; it is about 0.076 and 0.025 for $c_1/s_0=3.0$ and 5.0, respectively, for $v_r=0.4V_p$. The field observations of Vermilye & Scholz (1998) also suggest positive scaling between the width of the fracture zone and the fault length. It is not, however, straightforward to compare our simulation results with their field observations, partly because natural fracture zones will have been formed by repeated earthquakes on the same fault.

The fracture zone was formed predominantly on the dilational side of the main crack in the simulations shown above. Field observations, however, indicate that microfractures are distributed on both sides of faults (Anders & Wiltschko 1994; Vermilye & Scholz 1998), while the width of the fracture zone and the density of distributed microcracks are observed to be greatest on the dilational sides of faults (Reches & Lockner 1994; Knott *et al.* 1996). It is easy to visualize from our simulation results shown above that microcracks distributed on both sides of a fault will be formed by repeated earthquakes if each event nucleates at a different location on the same fault. Our simulations show another possibility for the formation of microcracks on both sides of faults. The fracture zone expands abruptly even on the compressive side when the crack tip velocity is reduced discontinuously. The expansion of the fracture zone is shown to be larger when the reduction in the crack tip velocity is larger; hence, the expansion will be largest when the crack tip growth is arrested abruptly (see Fig. 8). This is related to the radiation of elastic waves at the instant of discontinuous change in the crack tip velocity.

Since the shear stress is highly enhanced near the tip of the main crack, even after the termination of the crack tip growth, and dense microcracks are formed there as shown in Fig. 8, aftershocks are expected to cluster near the edge of the main crack; these aftershocks are caused by the dynamic coalescence of microcracks formed in zones near the arrested fault tips (Yamashita & Knopoff 1987, 1992). Takeo & Mikami (1990) and Hirata *et al.* (1996) showed from seismological observations that relatively large aftershocks tend to take place along the edges of regions of large fault slips. If the dynamic nucleation of the shear rupture is associated with the build-up of high-pressure fluids, the fluids will migrate efficiently in the fracture zone because the permeability is generally increased by the generation of tensile microcracks. The migrating fluid will promote the occurrence of aftershocks in the fracture zone, especially near the arrested rupture tips, by reducing the effective confining pressure (Yamashita 1998, 1999).

Slight expansion of the fracture zone also takes place on the compressive side when the crack tip velocity increases discontinuously, but the contraction is observed to occur on the dilational side. This contraction will occur because the fracture zone width is generally smaller for a larger crack tip velocity.

EFFECTS OF GENERATED MICROCRACKS ON RADIATED ELASTIC WAVES

Fig. 9 illustrates displacement waves observed at locations $(X_1/dX, X_3/dX)=(150, \pm 10)$ and $(150, \pm 80)$ for $c_1/s_0=2.0$ and ∞; ε_0 is fixed at 0.05 for the example with $c_1/s_0=2.0$. The tips of the main crack are assumed to extend with a fixed velocity of $0.4V_p$. The stations at (150, 10) and (150, ± 80) are outside the fracture zone throughout the calculated time period $0\leq T/dT\leq 2500$, while microcracks begin to be generated at $T/dT=884.0$ at location (150, -10). The microcrack density increases monotonically with time at location (150, -10) and attains the upper limit 0.05 at $T/dT=980.0$. It is seen in Fig. 9 that the difference in the radiated waves between the models with $c_1/s_0=2.0$ and ∞ tends to increase with time; the difference is shown to be much more appreciable in the vertical component (Fig. 9b). It should also be noted that the effect of generated microcracks is significant on the vertical component even if stations are outside the fracture zone. The reduction in the amplitude of the vertical displacement component may occur because the majority of the microcracks make very large angles

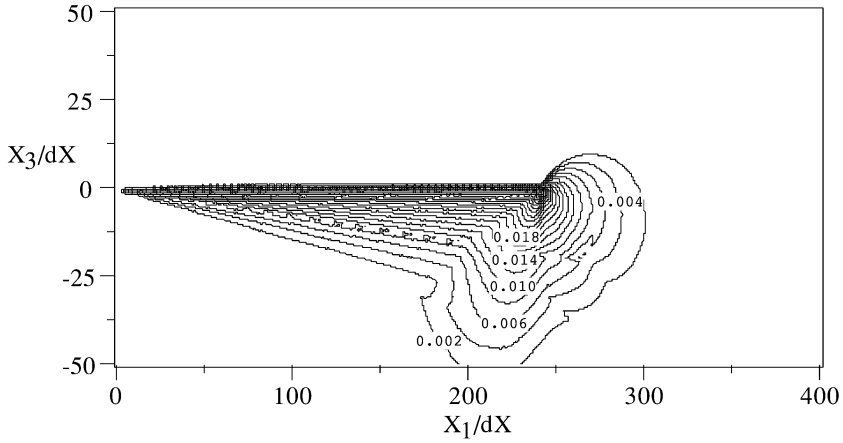

Figure 8. Distribution of microcrack density at $T/dT=2499$; the growth of the main crack with velocity $0.4V_p$ is assumed to be arrested abruptly when the tips arrive at $|X_1/dX|=240$. We assume $c_1/s_0=2.0$ and $\varepsilon_0=0.05$. Numerals indicate the distribution density of the microcracks.

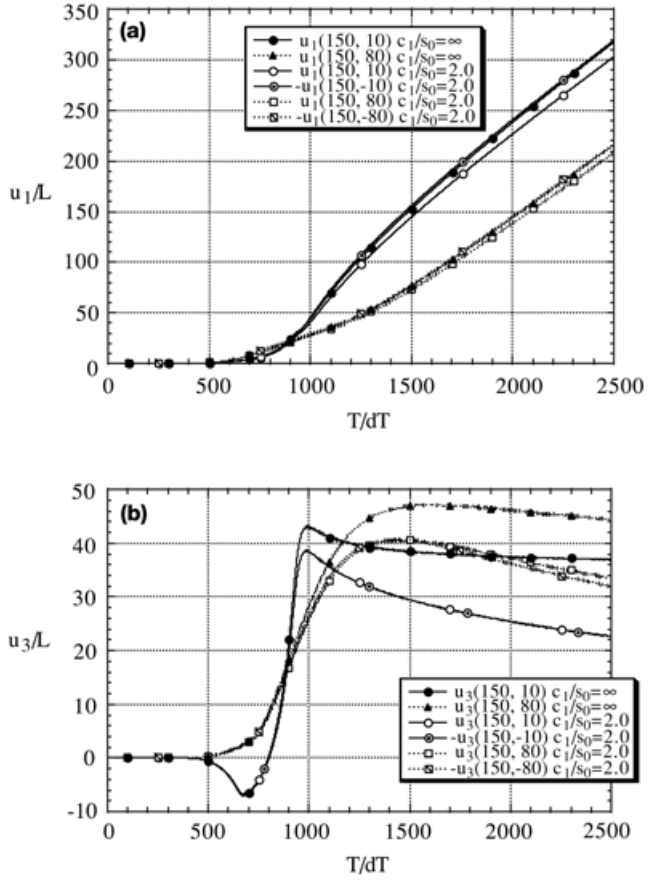

Figure 9. Dependence of (a) the X_1- and (b) the X_3-components of radiated displacement waves on the value c_1.

to the rupture plane, which causes contraction in the direction perpendicular to the rupture plane. Our calculations show that the difference from the waves radiated by a shear rupture embedded in an isotropic homogeneous medium is larger when ε_0 is larger or c_1/s_0 is smaller, while the effect of ε_0 is much more significant than that of c_1/s_0.

As shown above, when microcracks are generated, the vertical components of displacement waves recorded at near-field stations are very different from those expected from models of rupture embedded in an isotropic and homogeneous elastic medium. While the difference is rather small near the onset of the waves, it tends to increase with time. If the fracture zone is large or the microcrack density is high, this should be taken into account when we try to infer earthquake source process from the analysis of near-field seismic body waves: models of rupture embedded in an isotropic and homogeneous elastic medium are generally assumed in such studies. In other words, if later parts of the vertical component of displacement waves are dominant in the seismic wave data to be used for the analysis, it is likely that the inferred slip is very different from the actual slip.

RUPTURE GROWTH IN A FRACTURE ZONE

A majority of large earthquakes are known to occur in fractured zones, generally referred to as fault zones. Such fault zones may have been formed by repeated earthquakes on the same faults, as mentioned before. We now assume a large number of microcracks distributed in a zone $-H_p < X_3 + dX/2 < H_p$ before the dynamic nucleation of the main crack to simulate dynamic fault growth in a fault zone; the main crack is assumed to lie on the plane at $X_3/dX = -1/2$ as before. With regard to the orientations of these microcracks, only an idealized case is considered here: the pre-existing microcracks are assumed to be parallel to each other. Note that the spatial change in the orientation of microcracks should be smooth because of the assumption of Hudson's (1980) formula, which is exactly valid for aligned microcracks. We also assume that the density of the pre-existing microcracks, ε_p, decreases with distance from the plane of the main crack. We specifically assume the form $\varepsilon_p(X_3) = \varepsilon_0^p[1-(1+\alpha)|X_3+dX/2|/(\alpha|X_3+dX/2|+H_p)]$, where ε_0^p is the maximum density of the pre-existing cracks taken on the plane of the main crack; the density is assumed to vanish at $|X_3+dX/2| = H_p$. For $\alpha \simeq 10$, the decay of the microcrack density ε_p is approximated well by a logarithmic function of the distance from the plane of the main crack, so that we assume $\alpha = 10$ in the calculations. If several events occur repeatedly on the same plane and microcracks generated by each event have densities whose decays can be approximated by a logarithmic function of the distance from the rupture plane, then the decay of the total density can also be approximated by a logarithmic function. Hence, it is reasonable to assume a function such as the above one.

As stated above, here we assume the plane of the main crack to be at the centre of the fault zone. It is, however, suggested that some earthquakes occur along the interface between a fault zone and the country rock (e.g. Andrews & Ben-Zion 1997; Harris & Day 1997). We do not consider such a case here only because it is difficult to assume a sharp contrast in the effective elastic coefficients observed at the interface in the framework of our modelling: the perturbations of the elastic coefficients from the isotropic homogeneous case should be small enough in our modelling.

Fig. 10 shows the temporal change of the shear stress p_{31} immediately ahead of the propagating tip of the main crack on its plane. If this stress is lower, the crack tip growth tends to be more decelerated according to the shear traction fracture criterion. Since the orientation of the majority of microcracks generated by the rupture growth was shown to be in the range 110°–140° in the calculations above, we assume two models for the orientation of the pre-existing microcracks; all the pre-existing microcracks are assumed to be aligned in a single direction at $\theta = 110°$ or 140°. The upper threshold for the microcrack density is assumed to be 0.025 for both the pre-existing microcracks and the dynamically generated microcracks; the upper threshold of the total microcrack density, $\varepsilon_0 + \varepsilon_0^p$, is hence 0.05, which is in the range where the first-order perturbation is valid, as mentioned before. The effect of the pre-existing fracture zone width is investigated by assuming three values for H_p: $H_p/dX = 10$, 50 and 100. For comparison we also plot the result obtained when no pre-existing microcracks are assumed; the upper threshold for the distribution density of the dynamically generated microcracks is assumed to be 0.05 in this case, which is the same value assumed for the total microcrack density in the examples with the pre-existing fracture zone. The value of c_1/s_0 is fixed at 2.0 in all the calculated examples in Fig. 10.

We find in Fig. 10 that the crack tip shear stress is almost independent of the orientation of the pre-existing microcracks for a fixed value of H_p. This may reflect the fact that the

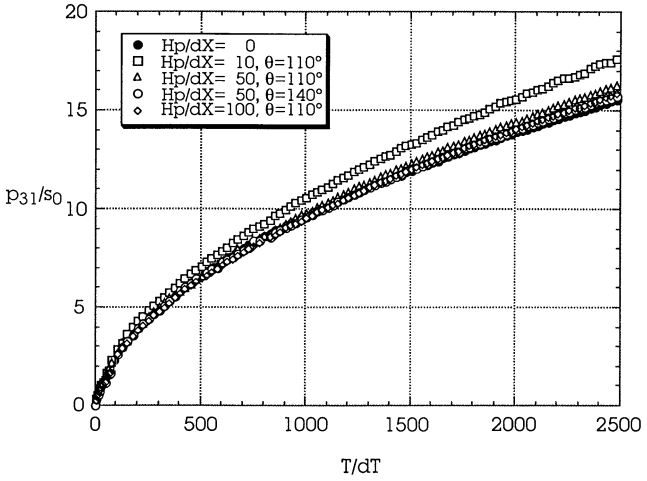

Figure 10. Temporal change of the shear stress at the tip of the crack dynamically extending in the pre-existing fracture zone. The orientation of the pre-existing microcracks is fixed at 110° or 140°; the width of the pre-existing fracture zone, $2H_p$, is in the range 20–200. The result obtained for the crack extending without a pre-existing fracture zone is also shown for reference. The main crack is assumed to extend with velocity $v_r/V_p=0.4$.

orientation of the majority of dynamically generated microcracks is in a rather narrow range from $\theta=110°$ to 140°. We also find a slight tendency for the crack tip shear stress to decrease with increasing H_p, while it is almost insensitive to the change in H_p for $H_p/dX>50$. This may occur because a region of higher microcrack density, which is given by the intersection of the pre-existing fracture zone and the distribution zone of dynamically generated microcracks, has a strong effect on the change in crack tip shear stress. This intersection is completely included in the pre-existing fracture zone when the width of the pre-existing fracture zone is large enough; the simulation results are not affected much by H_p in such a case. Note that we obtain $H_d/2dX\simeq50$ at $T/dT\simeq2500$ in our simulation with $c_1/s_0=2.0$ (see Fig. 3), so that the intersection is almost completely included in the pre-existing fracture zone in the time range $0\leq T/dT\leq2500$ for $H_p/dX=50\simeq100$. This is the reason why the crack tip shear stress is almost independent of H_p for $H_p/dX>50$. Fig. 10 also shows that there is little difference between the three curves with $H_p/dX=50\sim100$ and the curve with no pre-existing microcracks. This occurs because the orientations of dynamically generated microcracks are distributed in a rather narrow range from 110° to 140°, and because the intersection of the pre-existing fracture zone and the distribution zone of dynamically generated microcracks has a strong effect on the crack tip shear stress. It is also shown in our simulations that the crack tip shear stress is lower when the total microcrack density is higher. Hence, we can conclude from these observations that the crack tip shear stress is most sensitive to the dimension of the intersection and to the total microcrack density there.

DISCUSSION AND CONCLUSIONS

Our study provides the first detailed numerical simulation of the effects of generated tensile microcracks on dynamic rupture growth and radiated elastic waves. Earlier studies on the generation of microcracks were based on quasi-static analyses (Vermilye & Scholz 1998; Reches & Lockner 1994). In addition, they inferred only the orientations of the microcracks from the analysis of quasi-static tensile stresses; they did not consider embedded media with distributed microcracks. Dynamic analyses are indispensable for the investigation of radiated elastic waves. In addition, the abrupt expansion of the fault zone near the arrested crack tip (Fig. 8) is observed only by dynamic analysis.

Vermilye & Scholz (1998) suggested that microfracturing begins when the shear stress reaches a critical dilatancy stress of about 50 per cent of the initial yield stress. If this is the case, the value of $c_1/s_0=2.0$, assumed in many numerical examples, may be too small from the viewpoint of quantitative application to actual earthquakes; note that the initial yield stress is in the range $0–20s_0$ in the time range $0\leq T/dT\leq2500$ (see Fig. 6a). We assumed such a small value for c_1/s_0 in many calculations because a larger fracture zone is obtained in a fixed time range for a small value of c_1/s_0, which facilitates the qualitative understanding of the effect of the fracture zone and can save computation time and memory.

While Hudson (1980, 1981) considered both dry and fluid-filled microcracks, we assumed only the former in our simulations. A fluid-filled microcrack is defined as one in which the shear traction on the crack is zero and the displacement discontinuity is confined to the transverse direction only, while a dry microcrack is one in which all components of the traction on the crack vanish. Hudson (1980, 1981) showed that the resulting anisotropy in elastic constants is generally different in both cases. Since the migration rate of fluids is much less than the dynamic growth rate of faults, it is very reasonable to assume dry cracks for microcracks generated by the dynamic growth of a fault. However, an earthquake fault zone is generally regarded as a fluid conduit, as mentioned above, and it is probable that some pre-existing microcracks are fluid-filled. The effects of such fluid-filled pre-existing microcracks should also be investigated in the future.

The separation distances of the microcracks should be much greater than the sizes of the microcracks under the condition of dilute microcrack concentration. It is hence required that wavelengths of a propagating elastic wave are greater than the separation distances when the formula of Hudson (1980) is applied. The variation of the wavefield is sufficiently smooth except in the immediate neighbourhood of the advancing tips of the main crack in our simulations, as shown in Fig. 9, so that this requirement is generally satisfied, as long as very small values are assumed for the sizes of the microcracks.

We find a zone near the propagating crack tip where the shear stress is largely reduced compared to that expected from models of rupture embedded in an isotropic and homogeneous elastic medium (Fig. 6). This zone resembles the breakdown zone postulated for shear cracks (e.g. Yamashita & Ohnaka 1991). In general, only the distribution of the shear stress is described in the breakdown zone, but our simulations indicate that the normal stress component has a characteristic distribution near the crack tip. Since the normal stress vanishes over the crack plane for a crack embedded in an isotropic homogeneous medium, the variation of the normal stress will be sensitive to the distribution of microcracks near the crack tip.

While our simulation has the limitation that the distribution of microcracks must be dilute, it is shown that such a

distribution of microcracks may greatly affect the growth process of shear rupture. In fact, the generation of microcracks with a density threshold $\varepsilon_0 = 0.05$ is shown to reduce the shear stress at the propagating crack tip by as much as 18 per cent compared to the case of the shear rupture growing in the uncracked medium. This suggests that the growth of a shear crack tends to be impeded by the generation of microcracks.

The spatial distribution of microcracks is shown to be in good agreement with field and laboratory observations; the microcracks on the dilational side of the shear rupture make larger angles to the rupture plane than those on the compressive side, which is consistent with laboratory observations. The decrease in the microcrack density is approximated well by a logarithmic function of the distance from the rupture plane.

The geometry of a fracture zone can change abruptly when the rupture tip velocity varies discontinuously. This may complicate the formation process of fault zones and cause fault zone expansion even on the compressive side of the rupture. When the rupture growth is arrested abruptly, a large fracture zone is formed near the arrested rupture tip; this zone can act as a source region for aftershocks.

Our simulations also show that the component of radiated displacement waves perpendicular to the rupture plane is significantly affected by the generation of microcracks. For example, the generation of microcracks with a density threshold of $\varepsilon_0 = 0.05$ can reduce the amplitude of the perpendicular component of the displacement wave by as much as 33 per cent compared to that radiated by a shear rupture growing in an isotropic homogeneous medium in the assumed range of the model parameters.

ACKNOWLEDGMENTS

This study was supported in part by a Grant-in-Aid from the Ministry of Education, Science, Sports and Culture of Japan (project 08248111). Careful and constructive reviews by A. T. Gangi, R. Gibson and F. Chester helped to improve this manuscript.

REFERENCES

Alterman, Z., Burridge, R. & Loewenthal, D., 1971. The vibration of an elastic plane and half plane due to the sudden appearance of a crack, *Geophys. J. R. astr. Soc.,* **25,** 239–259.

Anders, M.H. & Wiltschko, D.V., 1994. Microfracturing, paleostress and the growth of faults,, *J. struct. Geol.,* **16,** 795–815.

Andrews, D.J. & Ben-Zion, Y., 1997. Wrinkle-like slip pulse on a fault between different materials, *J. geophys. Res.,* **102,** 553–571.

Boore, D.M., 1972. Finite-difference methods for seismic wave propagation in heterogeneous materials, in *Methods in Computational Physics,* Vol. 2, pp. 1–37, eds Alder, B., Fernbach, S. & Rotenberg, M., Academic Press, New York.

Burridge, R., 1969. The numerical solution of certain integral equations with non-integrable kernels arising in the theory of crack propagation and elastic wave diffraction, *Phil. Trans. R. Soc., Lond.,* A**265,** 353–381.

Caine, J.S., Evans, J.P. & Forster, C.B., 1996. Fault zone architecture and permeability structure, *Geology,* **24,** 1025–1028.

Chester, F.M., Evans, J.P. & Biegel, R.L., 1993. Internal structure and weakening mechanism of the San Andreas fault, *J. geophys. Res.,* **98,** 771–786.

Engelder, J.T., 1974. Cataclasis and the generation of fault gouge, *Geol. Soc. Am. Bull.,* **85,** 1515–1522.

Gangi, A.F., Min, K.D. & Logan, J.M., 1977. Experimental folding of rocks under confining pressure: Part IV—theoretical analysis of faulted drape-folds, *Tectonophysics,* **42,** 227–260.

Harris, R.A. & Day, S.M., 1997. Effects of a low-velocity zone on a dynamic rupture, *Bull. seism. Soc. Am.,* **87,** 1267–1280.

Hirata, N. *et al.*, 1996. Urgent joint observation of aftershocks of the 1995 Hyogo-ken Nanbu earthquake, *J. Phys. Earth,* **44,** 317–328.

Hudson, J.A., 1980. Overall properties of a cracked solid, *Math. Proc. Camb. Phil. Soc.,* **88,** 371–384.

Hudson, J.A., 1981. Wave speeds and attenuation of elastic waves in material containing cracks, *Geophys. J. R. astr. Soc.,* **64,** 133–150.

Hudson, J.A. & Crampin, S., 1991. On: A calculus for finely layered anisotropic media by M. Shoenberg & F. Muir, *Geophysics,* **56,** 572–576.

Kame, N. & Yamashita, T., 1997. Dynamic nucleation process of shallow earthquake faulting in a fault zone, *Geophys. J. Int.,* **128,** 204–216.

Kame, N. & Yamashita, T., 1999. A new light on arresting mechanism of dynamic earthquake faulting, *Geophys. Res. Lett.,* **26,** 1997–2000.

Kame, N. & Yamashita, T., 1999. Simulation of the spontaneous growth of a dynamic crack without constraints on the crack tip path, *Geophys. J. Int.,* **139,** 345–358.

Kelly, K.R., Ward, R.W., Treitel, S. & Alford, R.M., 1976. Synthetic seismograms: a finite-difference approach, *Geophysics,* **41,** 2–27.

Knott, S.D., Beach, A., Brockbank, P.J., Brown, J.L., McCallum, J.E. & Welbon, A.I., 1996. Spatial and mechanical controls on normal fault populations, *J. struct. Geol.,* **18,** 359–372.

Kostrov, B.V., 1964. Selfsimilar problems of propagation of shear cracks, *J. appl. Math. Mech.,* **28,** 1077–1087.

Moore, D.E. & Lockner, D.A., 1995. The role of microcracking in shear-fracture propagation in granite, *J. struct. Geology,* **17,** 95–114.

Petit, J.-P. & Barquins, M., 1988. Can natural faults propagate under mode II conditions?, *Tectonics,* **7,** 1243–1256.

Reches, Z. & Lockner, D.A., 1994. Nucleation and growth of faults in brittle rocks, *J. geophys. Res.,* **99,** 18 159–18 173.

Scholz, C.H., Dawers, N.H., Yu, J.-Z. & Anders, M.H., 1993. Fault growth and fault scaling laws: preliminary results, *J. geophys. Res.,* **98,** 21 951–21 961.

Takeo, M. & Mikami, N., 1990. Fault heterogeneity of inland earthquakes in Japan, *Bull. Earthq. Res. Inst.,* **65,** 541–569.

Tchalenko, J.S., 1970. Similarities between shear zones of different magnitudes, *Geol. Soc. Am. Bull.,* **81,** 1625–1640.

Tchalenko, J.S. & Berberian, M., 1975. Dasht-e Bayez fault, Iran: earthquake and earlier related structures in bed rock, *Geol. Soc. Am. Bull.,* **86,** 703–709.

Vermilye, J.M. & Scholz, C.H., 1998. The process zone: a microstructural view of fault growth, *J. geophys. Res.,* **103,** 12 223–12 237.

Yamashita, T., 1998. Simulation of seismicity due to fluid migration in a fault zone, *Geophys. J. Int.,* **132,** 674–686.

Yamashita, T., 1999. Pore creation due to fault slip in a fluid-permeated fault zone and its effect on seismicity, *Pure appl. Geophys.,* **155,** 625–647.

Yamashita, T. & Knopoff, L., 1987. Models of aftershock occurrence, *Geophys. J. R. astr. Soc.,* **91,** 13–26.

Yamashita, T. & Knopoff, L., 1992. Model for intermediate-term precursory clustering of earthquakes, *J. geophys. Res.,* **97,** 19 873–19 879.

Yamashita, T. & Ohnaka, M., 1991. Nucleation process of unstable rupture in the brittle regime: a theoretical approach based on experimentally inferred relations, *J. geophys. Res.,* **96,** 8351–8367.

APPENDIX A: ACCURACY OF THE METHOD

Our method of analysis is corroborated by comparing our numerical solution for the self-similar crack growth problem with the analytical solution. The exact analytical solution for dynamically propagating cracks with finite extent is available only in the self-similar crack problem, where a straight crack begins to form at the instant $T=0$ and then propagates along the X_1-axis bilaterally from the origin with a fixed rupture velocity. The remotely applied shear stress s_0 is assumed to be released completely on the crack surface; the medium is now assumed to be isotropic and homogeneous. The solution for this class of self-similar problem is given by Kostrov (1964).

The variations of relative slip, $\triangle u_1$, and the p_{31} component of the stress tensor are shown in Fig. A1 as functions of T at several locations on the X_1-axis. The rupture velocity is fixed at $0.4V_p$ ($=0.69V_s$), where V_p and V_s are the P- and S-wave velocities of the medium. The relative slip follows the analytical solution very closely. The numerical solution, however, has a smoother onset of slip, which is because of numerical dispersion and the calculation of the displacement not exactly on the crack but slightly off it. Finite difference calculations cannot reproduce the shear stress singularity at the crack tip, as typically observed in Fig. A1(b), because of the averaging of the stress concentration and numerical dispersion. A stress peak observed ahead of the crack tip is associated with the S-wave front.

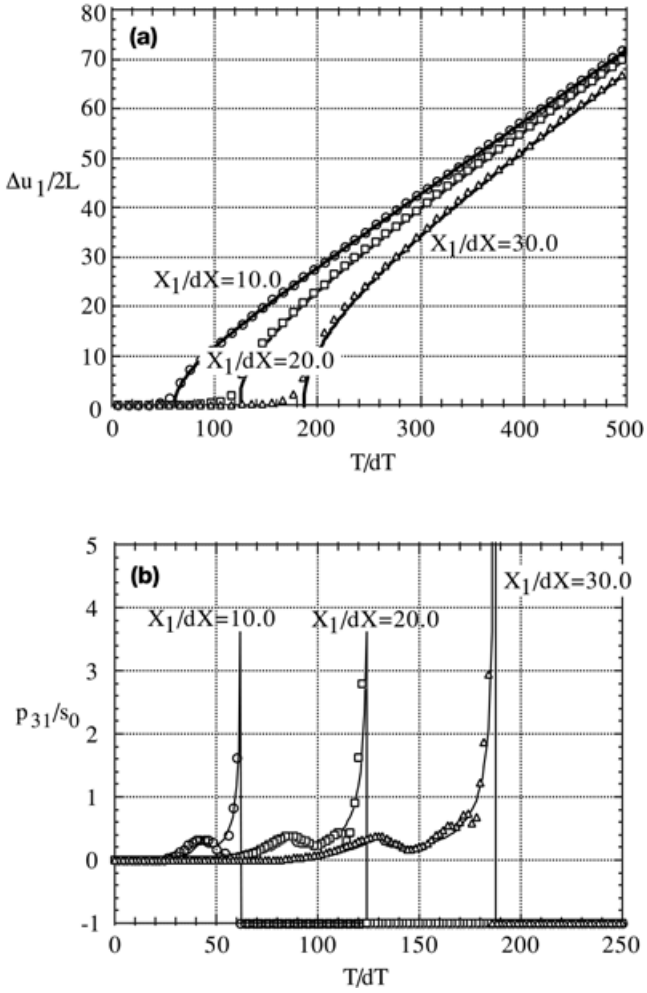

Figure A1. Comparison of the numerical and analytical solutions for the self-similar dynamic crack growth problem in (a) time evolution of the slip $\triangle u_1$ and (b) time evolution of the shear stress p_{31}. The solid curves denote the analytical solutions, and the numerical solutions are given by symbols.